ENCIT 2018

ABCM Associação Brasileira de Engenharia e Ciências Mecânicas

17th Brazilian Congress of Thermal Sciences and Engineering
November 25th-28th, 2018, Águas de Lindóia, SP, Brazil

ENCIT-2018-0820
NUMERICAL SIMULATION OF EXTRUDATE SWELL OF OLDROYD-B FLUIDS

Caroline Viezel
Murilo Francisco Tomé
Department of Applied Mathematics and Statistics, University of São Paulo, Av. Trabalhador São Carlense, 400, São Carlos, Brazil
cviezel@usp.br, murilo@icmc.usp.br

Abstract. *The objective of this work is to present numerical results of the extrudate swell problem of Oldroyd-B fluids employing arbitrary viscosity ratios* $\beta \in [0,\ 1]$. *To this effect, we formulated a finite difference method to solve the governing equations whereby the mass conservation, momentum and constitutive equations are solved implicitly on a staggered mesh. In this work, the extra-stress tensor* $\boldsymbol{\tau}$ *is computed via the conformation tensor which is solved by a semi-implicit method while the implicit Euler method is applied to solve the momentum equation. Analytic solutions for steady state tube flow are used to verify the Oldroyd-B code. To demonstrate the convergence of the numerical method on free surface flows, the extrudate swell was simulated on several refined meshes and details of the numerical solutions are presented. Moreover, by making* $\beta \to 0$, *the convergence of the Oldroyd-B model to the Upper-Convected-Maxwell model, on this complex free surface flow problem, is demonstrated.*

Keywords: *Die-swell, Oldroyd-B model, EVSS transformation, Conformation tensor, Finite difference.*

1. INTRODUCTION

Many industrial applications involve flows of viscoelastic materials in complex production lines as for example filling of containers in the food and cosmetic industries. These flows have attracted many researchers making the area of numerical solution of viscoelastic flows responsible for intense activity in the past decades. The problems studied include confined flows (Rajagopalan *et al.*, 1990; Wang, 2013; Ferrás *et al.*, 2014; Alves *et al.*, 2003) and free surface flows (e.g. Crochet and Keunings (1982); Russo and Phillips (2010); Castillo *et al.* (2015); Konaganti *et al.* (2015); Comminal *et al.* (2017); Tomé *et al.* (2016); Ren *et al.* (2015); Sadek and Yildiz (2013); Xu and Yu (2018)). These problems can be modelled either by the use of partial differential equations, called *differential constitutive models* or using integral equations, named *integral constitutive models* or still a mixed of both, the so called *integro-differential* models. However, the majority of the research on viscoelastic flows employ differential constitutive models and in particular, the Oldroyd-B model has been the differential model most studied. This model has attracted the investigators because it is difficult to tackle and there are many experimental and numerical (Sridhar *et al.*, 1986; Boger and Walters, 2012; Housiadas *et al.*, 2007; Xue *et al.*, 1998; Aboubacar and Webster, 2001; Brasseur *et al.*, 1998; Bonito *et al.*, 2006) results available in the literature that can be used to verify new techniques for simulating viscoelastic flows. Many investigators employ Eulerian methods and use the primitive variable formulation of velocity and pressure together with a decoupling strategy to calculate the velocity and pressure fields. Examples of these techniques are projection methods, SIMPLE, PISO, among others. Apart from these techniques, stream function formulations have been used to simulate confined flows (Choi *et al.*, 1988; Kupferman, 2001; Tian and Yu, 2011) and more recently were applied to solve free surface flows (e.g. Comminal *et al.* (2017)). However, the difficulties in applying the stream function to simulate three-dimensional flows has made this approach less attractive so that the primitive variable formulation has been used to simulate viscoelastic free surface flows.

The fluid free surface can be tackled by several techniques, for instance the Volume-of-Fluid (VOF) method that was introduced by Hirt and Nichols (1981) in the early 80's and has been used to simulate non-Newtonian flows by many investigators in the past 20 years (e.g. Kim and Lee (2003); Bonito *et al.* (2006); Janßen *et al.* (2013); Zhang (2013); Moraga *et al.* (2015); Comminal *et al.* (2017)). This method has the advantage of easy implementation but it is known of being a high diffusion technique so several improved versions have been developed (Kim and Lee, 2003; Zhang, 2013; Figueiredo *et al.*, 2016). Another approach to represent the free surface is the level set function. This function is convected with the fluid flow and its evolution in time is effected by solving a hyperbolic equation. Generally, this function is treated as a distance function from the interface. This method was introduced by Osher and Sethian (1988) and has capacity of capturing multiphase flow phenomena. It has been used to simulate filament stretching and jet buckling (Deganello *et al.*, 2011; Ville *et al.*, 2011; Castillo *et al.*, 2015), mold filling (Zhuang *et al.*, 2017) among other problems (Osher and

Fedkiw, 2001; Sussman *et al.*, 1994; Kohno and Tanahashi, 2004; Sethian, 2001; Dou *et al.*, 2007; Zhuang *et al.*, 2017). Different from VOF and the level set method, the front tracking method employs markers to describe the fluid interface. In two-dimensions the interface is represented by a set of points (x_i, y_i) that represents the interface between two fluids while in three dimensions the markers are nodes that define quadrilaterals or nodes defining triangles. The co-ordinates of the markers are updated continuously according to the instantaneous velocity of the fluid. In two-dimensions the interface is visualized by connecting these points by straight lines or a zero-order spline while in three dimensions the interface is composed of linear by parts quadrilaterals and triangles. The first ideas of this method was presented by Harlow and Welch (1965) who introduced the Marker-and-Cell method in the early 60's. Since its discovery, other improved versions have been developed and used by many authors to simulate free surface flows of Newtonian and non-Newtonian flows in two and three dimensions (see for example, Tomé *et al.* (2016); Amsden and Harlow (1970); Tomé *et al.* (2007); Harlow and Welch (1965); Tryggvason *et al.* (2001); Irfan and Muradoglu (2017); Pivello *et al.* (2014); Muradoglu and Tasoglu (2010); Wang *et al.* (2017); Yi *et al.* (2016); Terashima and Tryggvason (2009); Tomé *et al.* (2012)).

This work deals with the numerical solution of the Oldroyd-B model for free surface flows using the finite difference method on a staggered grid. The fluid free surface is tracked by an improved marker-and-cell type method that was presented by Tomé *et al.* (2000). The main feature of the technique employed is the use of a stress splitting (Rajagopalan *et al.*, 1990) that is independent of the viscosity ratio $\beta = \eta_S/\eta_0$ to obtain the solution of the momentum equations and to tackle the free surface boundary conditions. The extra-stress tensor is calculated employing the usual rheological splitting $\boldsymbol{\tau} = \boldsymbol{\tau}_P + 2\eta_S\,\mathbf{D}$ and is computed as a function of the conformation tensor $\mathbf{A}$. Results are presented for the extrudate swell problem.

2. BASIC EQUATIONS

The mass conservation and momentum equations for incompressible viscoelastic fluid flows can be written as,

$$\nabla \cdot \mathbf{u} = 0\,, \tag{1}$$

$$\rho\Big[\frac{\partial \mathbf{u}}{\partial t} + \nabla\cdot(\mathbf{uu})\Big] = -\nabla p + \nabla\cdot\boldsymbol{\tau} + \rho\mathbf{g}\,, \tag{2}$$

where $\mathbf{u}$ is the velocity vector, p is the pressure, $\mathbf{g}$ is the acceleration of gravity vector, ρ is the density of the fluid and $\boldsymbol{\tau}$ is the extra-stress tensor. It is assumed that the flow is governed by the Oldroyd-B constitutive equation which is given by

$$\boldsymbol{\tau} + \lambda_1 \overset{\nabla}{\boldsymbol{\tau}} = 2\eta_0\,\left[\mathbf{D} + \lambda_2 \overset{\nabla}{\mathbf{D}}\right], \qquad \mathbf{D} = \frac{1}{2}\Big[(\nabla\mathbf{u}) + (\nabla\mathbf{u})^T\Big]\,, \tag{3}$$

where $\mathbf{D}$ is the rate-of-deformation tensor. The symbol $\overset{\nabla}{\boldsymbol{\tau}}$ represents the upper-convected derivative given by

$$\overset{\nabla}{\boldsymbol{\tau}} = \frac{\partial\boldsymbol{\tau}}{\partial t} + \nabla\cdot(\mathbf{u}\boldsymbol{\tau}) - \big(\nabla\mathbf{u}\big)\boldsymbol{\tau} - \boldsymbol{\tau}\big(\nabla\mathbf{u}\big)^T.$$

In Eq. (3), λ_1 is the relaxation time, $\lambda_2 = \lambda_1\dfrac{\eta_S}{\eta_0}$ is the retardation time, $\eta_0 = \eta_P + \eta_S$ is the sum of the solvent (η_S) and polymeric (η_P) viscosities. The ratio $\beta = \dfrac{\eta_S}{\eta_0}$ measures the quantity of solvent viscosity within the fluid. When $\beta = 0$, Eq. (3) reduces to the *Upper-Convected Maxwell* (UCM) model and if $\beta = 1$ we have *Newtonian* flow.

To solve the momentum Eq. (2), we employ the following transformation (known as EVSS (Rajagopalan *et al.*, 1990; Guénette and Fortin, 1995))

$$\boldsymbol{\tau} = \mathbf{T} + 2\eta_0\mathbf{D}\,, \tag{4}$$

which after being introduced in the momentum Eq. (2), it becomes

$$\rho\Big[\frac{\partial \mathbf{u}}{\partial t} + \nabla\cdot(\mathbf{uu})\Big] = -\nabla p + \eta_0\nabla^2\mathbf{u} + \nabla\cdot\mathbf{T} + \rho\mathbf{g}\,. \tag{5}$$

Instead of solving the Oldroyd-B constitutive equation, we write the extra-stress tensor $\boldsymbol{\tau}$ using the conformation tensor $\mathbf{A}$ by

$$\boldsymbol{\tau} = \frac{\eta_0}{\lambda_1}\big(1-\beta\big)\big(\mathbf{A}-\mathbf{I}\big) + 2\beta\eta_0\,\mathbf{D}\,, \tag{6}$$

where the conformation tensor $\mathbf{A}$ is evolved in time by solving

$$\mathbf{A} + \lambda_1\overset{\nabla}{\mathbf{A}} = \mathbf{I}\,. \tag{7}$$

2.1 Boundary conditions

The boundary conditions can be summarized as follows: on rigid boundaries the no-slip condition is imposed; on inflows, the velocity is prescribed while the extra-stress tensor obeys fully developed flow. On outflows, homogeneous Neumann conditions are imposed for the velocity field. On the free surface, in the absence of surface tension, the boundary conditions are given by equations

$$\mathbf{n}^T \cdot (\boldsymbol{\sigma} \cdot \mathbf{n}) = 0\,, \qquad \mathbf{m}^T \cdot (\boldsymbol{\sigma} \cdot \mathbf{n}) = 0\,, \tag{8}$$

where, $\boldsymbol{\sigma} = -p\mathbf{I} + \mathbf{T} + 2\eta_0\mathbf{D}$ is the stress tensor and $\mathbf{n}$ and $\mathbf{m}$ are unity vectors normal and tangential to the free surface, respectively.

2.2 NUMERICAL METHOD

The Equations (1), (5), (6), (7) and (4) are solved by the finite difference method on a staggered grid (Fig. 1a displays an example of a staggered cell). The fluid (also the free surface) is modeled by an improved Marker-and-Cell method (Amsden and Harlow, 1970) developed by Tomé *et al.* (2000) wherein the fluid surface is determined by a closed linear spline that is defined by the nodes defined by the marker-particles (see Fig. 1b). To implement this technique it is necessary to divide the cells within the mesh into several types: Boundary (**B**), Inflow (**I**), Outflow (**O**), Full (**F**), Surface (**S**) and Empty (**E**). Figure 1c displays an example of such cells.

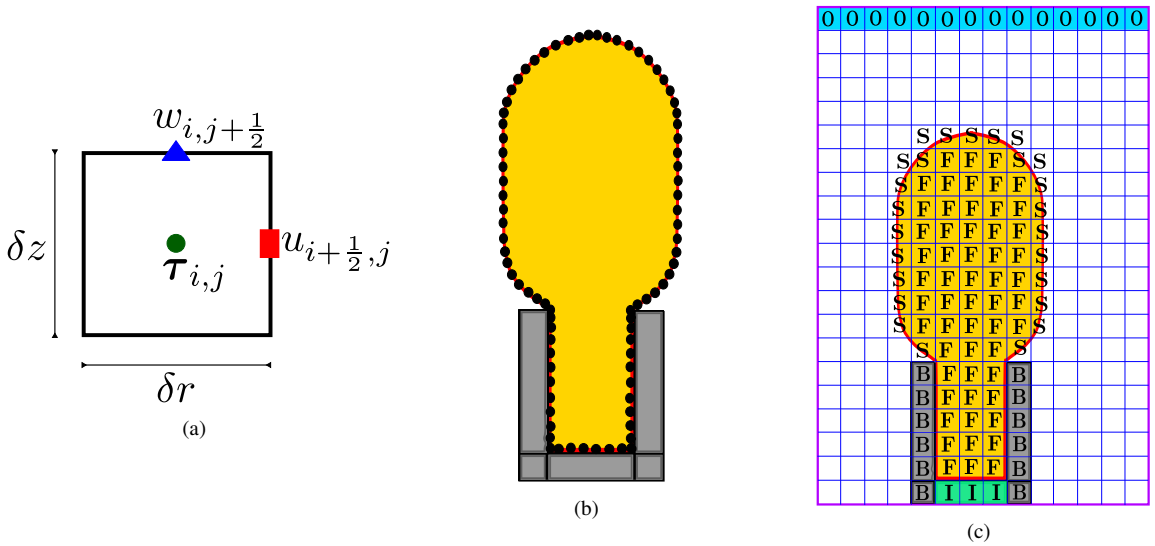

Figure 1: (a) Example of a staggered cell in the mesh. (b) Representation of fluid free surface (line connecting the particles) and volume of fluid (yellow area). (c) Type of cells in the domain.

Let δt be specified and $t_{n+1} = t_n + \delta t$. Then, Eqs. (1), (5), (6), (7) and (4), written in cylindrical coordinates, can be solved for the unknowns $\mathbf{u}^{n+1} = \mathbf{u}(r, z, t_{n+1}))$, $p^{n+1} = p(r, z, t_{n+1})$, $\mathbf{T}^{n+1} = \mathbf{T}(r, z, t_{n+1})$, $\boldsymbol{\tau}^{n+1} = \boldsymbol{\tau}(r, z, t_{n+1})$ and $\mathbf{A}^{n+1} = \mathbf{A}(r, z, t_{n+1})$, as follows. These equations are used in dimensionless form and contain the nondimensional numbers, *Reynolds* number: $Re = \dfrac{\rho_0\, U\, L}{\eta_0}$, *Weissenberg* number: $Wi = \lambda_1 \dfrac{U}{L}$, *Froude* number: $Fr = \dfrac{U}{\sqrt{L\, g}}$, in which L and U are typical scales for velocity and length, respectively, ρ_0 is the fluid density and g is the acceleration of gravity (for details see Tomé *et al.* (2007)).

The computational cycle is performed in three steps, as follows:

- **STEP 1:** The velocity $\mathbf{u}^{n+1}$ and the pressure p^{n+1} are computed using the implicit technique developed by Oishi *et al.* (2011). In this technique, a tentative velocity field $\widetilde{\mathbf{u}}^{n+1}$ is calculated from the momentum Eq. (5) using the implicit Euler method while the final velocity $\mathbf{u}^{n+1}$ is given by $\mathbf{u}^{n+1} = \widetilde{\mathbf{u}}^{n+1} - \nabla\psi$ where ψ is a potential function that is obtained by solving the Poisson equation $\nabla^2\psi = \nabla \cdot \widetilde{\mathbf{u}}^{n+1}$ to guarantee that $\nabla \cdot \mathbf{u}^{n+1} = 0$ within the fluid. The Poisson equation is solved by the conjugate gradient method subject to Dirichlet and Neumann boundary conditions. The pressure is calculated as $p^{n+1} = p^{(n)} + \dfrac{\psi}{\delta t} - \dfrac{1}{Re}\nabla^2\psi$.

  This technique is described in details by Oishi *et al.* (2011) and for this reason is not given here.

■ **STEP 2:** Calculation of $\boldsymbol{\tau}^{n+1}$, $\mathbf{A}^{n+1}$ and $\mathbf{T}^{n+1}$.

In this step we first calculate the conformation tensor $\mathbf{A}^{n+1}$ by solving Eq. (7) using finite differences. Equation (7) is implicitly approximated at the center of a cell (i,j) by the equation

$$\mathbf{A}_{i,j}^{n+1} - \delta t\Big[(\nabla \mathbf{u}_{i,j}^{n+1})\mathbf{A}_{i,j}^{n+1} + \mathbf{A}_{i,j}^{n+1}(\nabla \mathbf{u}_{i,j}^{n+1})^T - \frac{1}{Wi}\mathbf{A}_{i,j}^{n+1}\Big] = \mathbf{A}_{i,j}^{n} - \delta t\left[\nabla\cdot(\mathbf{u}_{i,j}^{n+1}\mathbf{A}_{i,j}^{n}) - \frac{1}{Wi}\mathbf{I}\right]. \quad (9)$$

which is applied to each **F** and **S** cell within the domain. This originates a (3×3) linear system that is solved for each **F** and **S**-cell.

After $\mathbf{A}^{n+1}$ has been calculated, the extra-stress tensor $\boldsymbol{\tau}_{i,j}^{n+1}$ is obtained by

$$\boldsymbol{\tau}_{i,j}^{n+1} = \frac{1}{Re\,Wi}(1-\beta)\left(\mathbf{A}_{i,j}^{n+1} - \mathbf{I}\right) + \frac{2}{Re}\beta\,\mathbf{D}_{i,j}^{n+1}, \quad (10)$$

and the non-Newtonian tensor $\mathbf{T}_{i,j}^{n+1}$ is computed from

$$\mathbf{T}_{i,j}^{n+1} = \boldsymbol{\tau}_{i,j}^{n+1} - \frac{2}{Re}\mathbf{D}_{i,j}^{n+1}. \quad (11)$$

■ **STEP 3:** The last step in the calculational cycle is to move the marker-particles to their new positions by solving

$$\frac{dr}{dt}\Big|_{\mathbf{P}} = u(r,z)_{\mathbf{P}}^{n+1}; \qquad \frac{dz}{dt}\Big|_{\mathbf{P}} = w(r,z)_{\mathbf{P}}^{n+1}, \quad (12)$$

for each particle $\mathbf{P} = [r_{\mathbf{P}}\ z_{\mathbf{P}}]^T$. The particle velocity $\mathbf{u_P} = [u(r,z)_{\mathbf{P}}^{n+1}\ v(r,z)_{\mathbf{P}}^{n+1}]^T$ is found by a bilinear interpolation using the nearest velocities and the ODE system is resolved by a second-order Runge-Kutta method (RK21). For details see Tomé *et al.* (2007) and Oishi *et al.* (2011).

3. VERIFICATION RESULTS

To verify the numerical method described in Section 2.2, fully developed tube flow was simulated and the numerical predictions were compared with the analytic solutions.

A tube of radius $R = 1.0$ m and length $H = 10R$ m composed the computational domain $\Omega = [0\,,\ R]\times[0\,,\ 10R]$ as illustrated in Fig. 2b. The tube was empty and fluid was injected at the inflow with the imposition of the following fully developed profile:

$$w(r) = \left(1 - r^2\right), \qquad u(r) = 0, \qquad \dot{\gamma} = \frac{dw}{dr} = -2r, \quad (13a)$$

$$\tau^{zz}(r) = \frac{2}{Re}Wi(1-\beta)\dot{\gamma}^2, \qquad \tau^{rz}(r) = \frac{1}{Re}\dot{\gamma}, \qquad \tau(r) = \tau^{\theta\theta}(r) = 0, \quad (13b)$$

The input data were: $L = R = 1$m, $U = 1$ms^{-1}, $\rho = 1000$kg m^{-3}, $\eta_0 = 4000.0$Pa.s, $\lambda_1 = 1.0$s and $\lambda_2 = 0.2$s ($\beta = 0.2$). Therefore, $Re = \dfrac{\rho\,U\,L}{\eta_0} = 0.25$ and $Wi = \lambda_1\dfrac{U}{L} = 1.0$. By using the meshes presented in Tab. 1, this problem was simulated until time $t(U/L) = 100.0$ on each mesh.

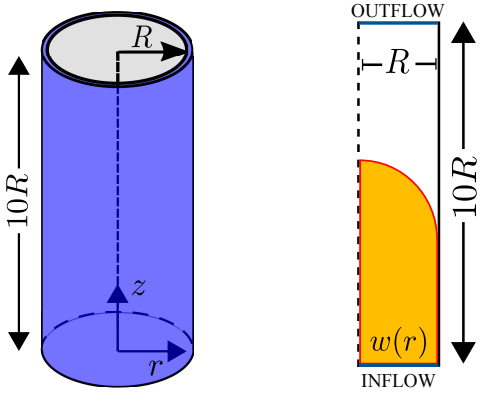

(a) (b)

Figure 2: Description of flow domain (a) and computational domain (b).

Table 1: Meshes used to simulate tube flow.

Mesh	M10	M20	M30	M40
$\delta_r = \delta_z$	0.1000	0.0500	0.0333	0.0250
Cells in the mesh	(10×100)	(20×200)	(30×300)	(40×400)
δt	6.25000e-05	1.56250e-05	3.47222e-06	1.95312e-06

Figure 3 displays the numerical solutions obtained for $w(r, z_m)$, $\tau^{zz}(r, z_m)$ and $\tau^{rz}(r, z_m)$ plotted at the cross section in the middle of the tube at $z_m = 5R$. For comparisons, the analytic solutions are also plotted in Fig. 3. It can be seen that the numerical solutions agree well with the corresponding analytic solutions on the meshes employed. Moreover, Tabs. 2 and 3 show that, the errors calculated with the norm defined by Eq. (14) decay with mesh refinement and the calculated convergence order is about two. This is in accordance with the second-order finite difference approximations employed to solve the equations.

$$E(\cdot)_{Mk} = \sqrt{\delta_k \sum_{i_{Mk}} \left[(\cdot)_{Exact} - (\cdot)_{Num}\right]^2}, \qquad (14)$$

$\delta_k = \delta r_{Mk}$, Mk denotes mesh M10, M20, M30, M40.

Table 2: Errors between analytic and numerical solutions calculated on meshes M10, M20, M30 and M40.

Mesh	$E(w(r, z_m))$	$E(\tau^{rz}(r, z_m))$	$E(\tau^{zz}(r, z_m))$
M10	1.6838260e-03	2.2804317e-02	1.1240207e-01
M20	4.2603404e-04	5.7499787e-03	2.8459013e-02
M30	1.8985006e-04	2.5595843e-03	1.2678808e-02
M40	1.0655251e-04	1.4404461e-03	7.1377747e-03

Table 3: Convergence order obtained on the *tube* flow.

	$w(r, z_m)$	$\tau^{rz}(r, z_m)$	$\tau^{zz}(r, z_m)$
O(M10,M20)	1.9827025e+00	1.9876785e+00	1.9817111e+00
O(M20,M30)	1.9934752e+00	1.9961059e+00	1.9940877e+00
O(M20,M40)	1.9994041e+00	1.9970409e+00	1.9953394e+00
O(M30,M40)	2.0077604e+00	1.9983588e+00	1.9971035e+00

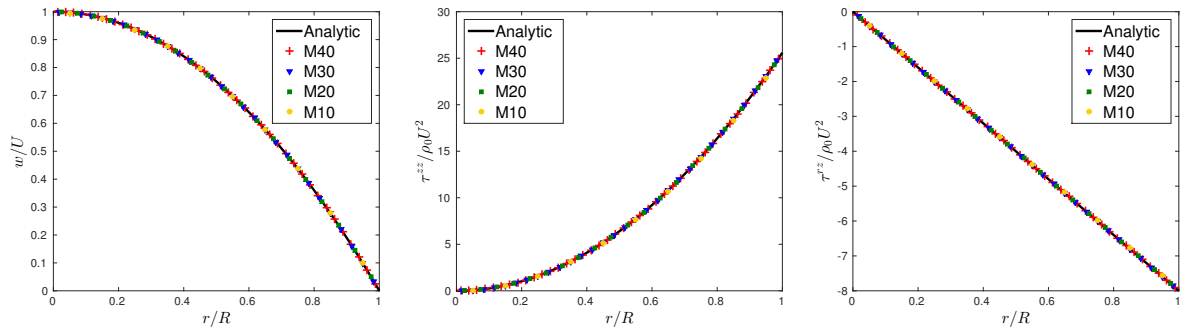

(a) (b) (c)

Figure 3: Comparison of the numerical predictions in the various meshes with the respective exact solutions: (a) $w(r)$; (b) $\tau^{zz}(r)$ and (c) $\tau^{rz}(r)$.

3.1 Numerical simulation of the die-swell phenomenon

A jet emerging from a tube exhibits the phenomenon known as *die-swell*, also called *extrudate swell* or *Barus effect* (see Fig. 4a), in which the diameter of the jet inside the tube (D) is expanded ($D_m > D$) after the jet is extruded into the air. This phenomenon is common in polymer processing and is associated with entropy and the relaxation of the polymer molecules within the flow stream. This problem has been investigated by many researchers that developed numerical tools to predict the amount of swell which is measured by the swelling ratio defined by $S_r = \dfrac{D_m}{D}$.

3.1.1 Mesh refinement

To simulate this problem, we considered the time-dependent flow of an axisymmetric jet that is flowing inside a tube and then is extruded into the air. The flow domain is displayed in Fig. 4b and the following input data were employed:

- computational domain: $\Omega = [0\,,\,3R] \times [0\,,\,15R]$;
- tube radius $R = 1.0\,\text{m}$, tube length $L_1 = 5R\,\text{m}$ and length scale: $L = R$;
- Distance between tube exit and the outflow region: $L_2 = 10R\,\text{m}$;
- $\rho = 1000\,\text{kg m}^{-3}$, $\eta_0 = 2000\,\text{Pa.s}$, $\lambda_1 = 1.0\,\text{s}$, $\lambda_2 = 0.1\,\text{s}$ and $U = 1.0\,\text{m}$;
- $Re = 0.5$, $Wi = 1.0$ and viscosity ratio: $\beta = 0.1$. Gravity was neglected.

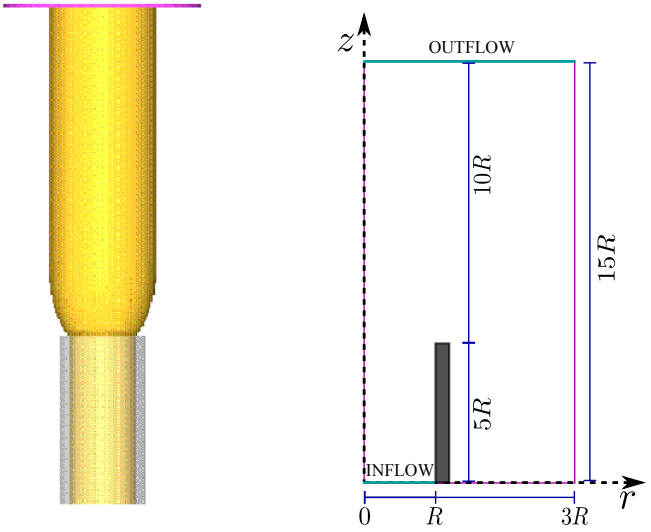

(a) (b)

Figure 4: Description of the computational domain for the simulation of die-swell.

The boundary conditions were those described in Section 2.1. The fully developed profile given by equations

$$w(r) = \frac{3}{2}[1 - r^2], \qquad u(r) = 0, \qquad \dot{\gamma} = \frac{dw}{dr} = -3r, \tag{15}$$

was specified at the inflow. The extra-stress tensor is specified in Eq. (13b).

To substantiate the code on this problem, we performed mesh refinement and simulated the die-swell on the grids defined in Tab. 4. These simulations started at $t = 0$ and were carried out until time $t = 200$s; at this time, it was assumed that steady state has been reached. Figure 5 displays the velocity $w(0.5\delta r, z)$ and the first normal stress difference $N_1 = (\tau^{zz} - \tau^{rr})(z)$ on the line $(0.5\delta r, z)$ on the meshes simulated. We can see that the numerical solutions obtained are in good agreement. It is also observed that on the tube exit, both the velocity and N_1 present an overshoot that is caused by the corner singularity on the tube exit (André and Clermont, 1987). The free surface profiles obtained are shown in Fig. 6 where it can be seen that the free surfaces on the coarse grids approximate the solution obtained on the finest grid M30, as the grid is refined. These results confirm the convergence of the numerical method and verifies our code on the die-swell problem.

Table 4: Meshes used to simulate die-swell flow.

Mesh	M10	M16	M20	M24	M30
$\delta_r = \delta_z$	0.10000	0.06250	0.05000	0.04166	0.03333
Cells in the mesh	(30×150)	(48×240)	(60×300)	(72×360)	(90×450)

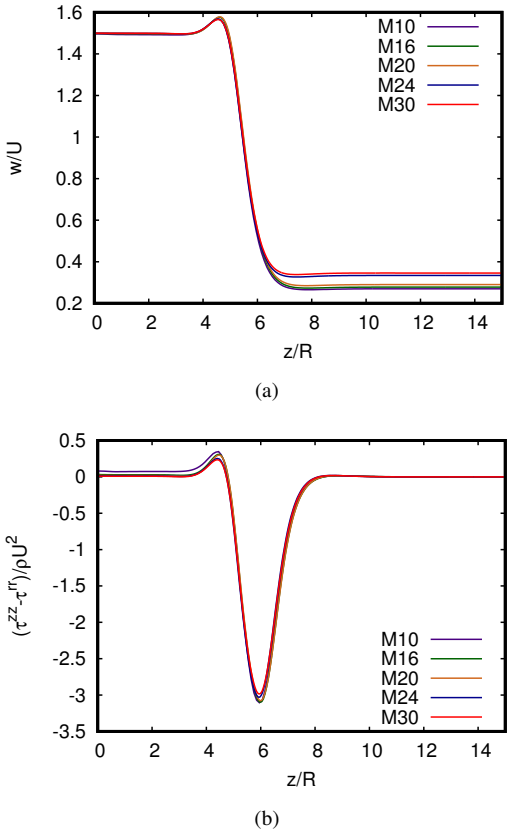

Figure 5: Simulation of die-swell on several meshes: (a) $w(0.5\delta r, z)$ and (b) $N_1(0.5\delta r, z)$. Results obtained on meshes M10, M16, M20, M24 and M30.

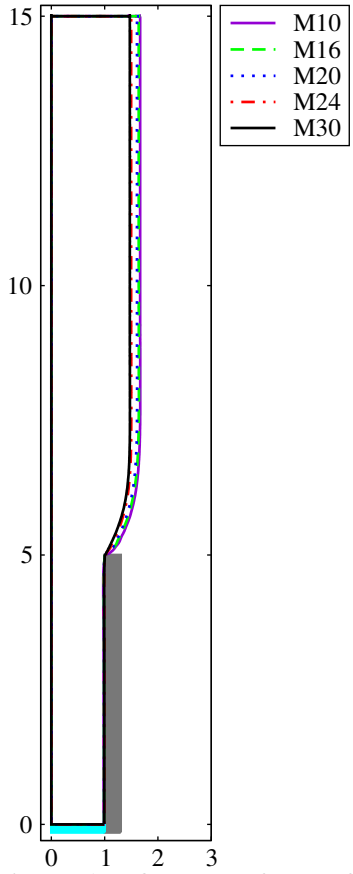

Figure 6: Mesh refinement: free surface obtained on each mesh.

3.1.2 Simulation of die-swell and comparison with results from literature

To demonstrate the applicability of the code on the die-swell problem, we performed a series of simulations varying the Weissenberg number Wi while keeping fixed the value of the Reynolds number. The flow domain and the input data were the same employed in the mesh refinement results (see Section 3.1.1, Fig. 4) together with mesh M10 (see Tab. 1). In these simulations we used $Re = 0.25$ and the following velocity profile was imposed at the tube entrance (the extra-stress components are specified according to Eq. 13b)

$$w(r) = 2[1 - r^2], \qquad u(r) = 0, \qquad \dot{\gamma} = \frac{dw}{dr}|_{wall} = -4. \tag{16}$$

With the purpose of making a comparison with results from literature, the simulations were carried out by varying the *recoverable shear* that was used in the works of Crochet and Keunings (1982), Tomé *et al.* (2007) and Tanner (1970), given by

$$S_\lambda = \frac{N_1}{2\tau^{rz}} = Wi(1-\beta)|\dot{\gamma}|_{wall} = 4\,(1-\beta)Wi. \tag{17}$$

The values of S_λ and the associated values of Wi for $\beta = 1/9$ employed in the simulations are displayed in Tab. 5 below.

Table 5: Values of the *recoverable shear* S_λ and corresponding $Wi = \lambda_1$ (since $L = U = 1$) calculated using Eq. (17) used in the die-swell simulations.

S_λ	0.5	1.0	1.5	2.0	2.5	3.0	3.5	4.0
$Wi = \lambda_1$	0.1406	0.2812	0.4219	0.5625	0.7031	0.8437	0.9844	1.1250

The simulations started at $t = 0$ and were performed until $t * (U/L) = 100$. At $t = 0$ the die was empty and was continuously filled until $t = 5$ when the jet is leaving the tube and being extruded in the air. After this time, the fluid started the swelling process which changed according to the value of S_λ. It is expected that larger values of S_λ will lead to larger swelling ratios S_r. Indeed, Fig. 7 displays a front view visualization of the simulation for $S_\lambda = 1.5$ while Fig. 8 presents the visualizations for $S_\lambda = 4$, at the selected times shown. At time $t = 5$ the results are similar for both values of S_λ but from time $t = 10$ the differences become more evident. After this time, it is seen that the jet with $S_\lambda = 1.5$ travels faster than the jet with $S_\lambda = 4$. This effect is due to the fact that the jet with $S_\lambda = 4$ presents a swell much larger than the swell corresponding to $S_\lambda = 1.5$ and consequently due to mass conservation, the jet with $S_\lambda = 1.5$ moves faster. Moreover, after entering the outflow region, both jets undergo a secondary swell (see $t = 25$ for $S_\lambda = 1.5$ and $t = 30$ for $S_\lambda = 4$) and it is seen that the jet with $S_\lambda = 1.5$ establishes steady state around $t = 50$ while the jet with $S_\lambda = 4$ seems to reach steady state around $t = 100$. The final swelling ratio obtained for each S_λ is displayed in Tab. 6 in which the results obtained by Crochet and Keunings (1982) and Tanner's law (see Eq. 18) are also shown for comparison. Finally, Fig. 9 plots the results of Tab. 6 together with the results obtained by Tomé *et al.* (2007). We can see in Fig. 9 that the results of this work agree better with Tomé et al. predictions for small values of S_λ and fits better Tanner's law and Crochet and Keunings for values of S_λ above 2.

$$S_r = 0.14 + \left[1.0 + \frac{S_\lambda^2}{2}\right]^{\frac{1}{6}} \tag{18}$$

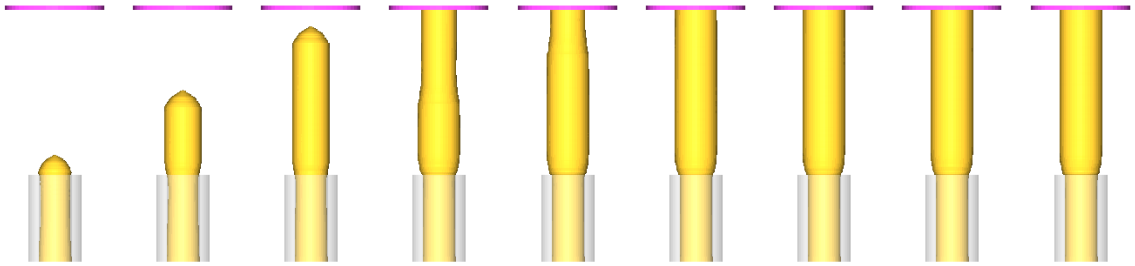

(a) t=5 (b) t=10 (c) t=15 (d) t=25 (e) t=30 (f) t=35 (g) t=40 (h) t=50 (i) t=100

Figure 7: Simulation of transient die-swell for $Re = 0.25, \beta = 1/9, S_\lambda = 1.5$ at selected times.

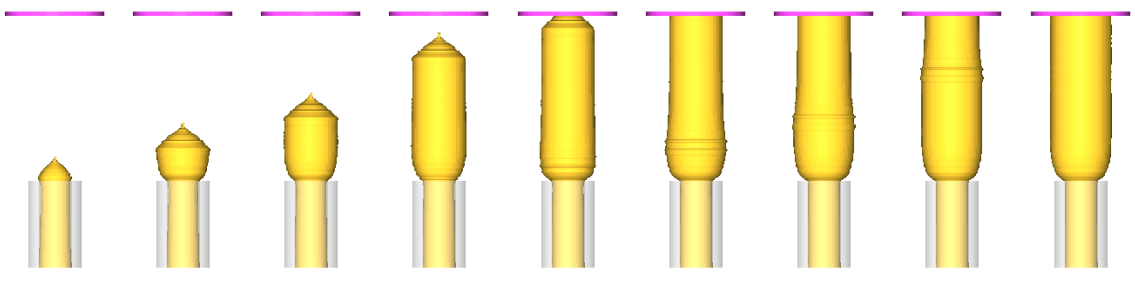

(a) t=5 (b) t=10 (c) t=15 (d) t=25 (e) t=30 (f) t=35 (g) t=40 (h) t=50 (i) t=100

Figure 8: Simulation of transient die-swell for $Re = 0.25, \beta = 1/9, S_\lambda = 4.0$ at selected times.

Table 6: Swelling ratios S_r obtained in the simulations and comparison with Tanner's law, Crochet and Keunings results.

S_λ	0.5	1.0	1.5	2.0	2.5	3.0	3.5	4.0
S_r (this work)	**1.2320**	**1.2770**	**1.3250**	**1.3870**	**1.4410**	**1.645**	**1.7000**	**1.7880**
S_r Crochet and Keunings (1982)	1.1573	1.2357	1.3035	1.3799	1.4762	1.5972	1.8001	1.9198
Tanner's law (Tanner, 1970)	1.1598	1.2099	1.2738	1.3409	1.4063	1.4685	1.5271	1.5822

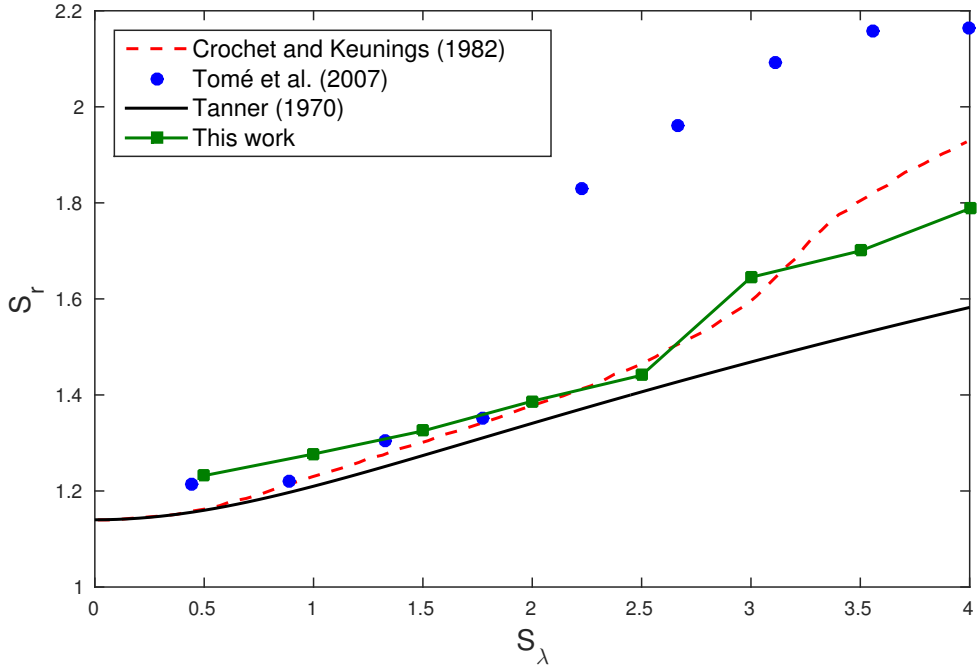

Figure 9: Simulation of transient die-swell for $Re = 0.25, \beta = 1/9$. Swelling ratios obtained by various authors.

4. CONCLUSIONS

This work presented a numerical technique for solving the Oldroyd-B model for time-dependent free surface flows. The methodology employs the marker-and-cell method to describe the fluid free surface and is based on the ideas employed by Tomé *et al.* (2007). The novelties of this technique are the use of an EVSS transformation that permits to solve the momentum and mass conservation equations without the appearance of the viscosity ratio β so that we can make $\beta = 0$ in the governing equations to solve the UCM model. Also, the extra-stress tensor is calculated as a function of the conformation tensor $\mathbf{A}$ that is approximated by finite difference equations that are solved exactly. This numerical technique was validated against analytic solutions for fully developed tube flow and mesh refinement confirmed the convergence of the method on this particular problem. The capability of this methodology in solving complex free surface flows was demonstrated by applying it to simulate the die-swell problem for various values of the Weissenberg number. Mesh refinement studies and comparison with other authors corroborated the efficiency of the method in dealing with complicated free surface flows.

5. ACKNOWLEDGEMENTS

The authors would like to acknowledge the financial support given by the funding agencies: CNPq - Conselho Nacional de Desenvolvimento Científico e Tecnológico Grant No. 306280/2014-0 and 150282/2017-6, FAPESP Grant No. 2013/07375-0 (CEPID-CeMEAI project) and CAPES Grant No. PROEX-9259544/D.

6. REFERENCES

Aboubacar, M. and Webster, M., 2001. "A cell-vertex finite volume/element method on triangles for abrupt contraction viscoelastic flows". *Journal of Non-Newtonian Fluid Mechanics*, Vol. 98, No. 2-3, pp. 83–106.

Alves, M.A., Oliveira, P.J. and Pinho, F.T., 2003. "Benchmark solutions for the flow of oldroyd-b and ptt fluids in planar contractions". *Journal of Non-Newtonian Fluid Mechanics*, Vol. 110, No. 1, pp. 45–75.

Amsden, A.A. and Harlow, F.H., 1970. "A simplified mac technique for incompressible fluid flow calculations". *Journal of computational physics*, Vol. 6, pp. 322–325.

André, P. and Clermont, J.R., 1987. "Numerical simulation of the die swell problem of a newtonian fluid by using the concept of stream function and a local analysis of the singularity at the corner". *Journal of Non-Newtonian Fluid Mechanics*, Vol. 23, pp. 335–354.

Boger, D.V. and Walters, K., 2012. *Rheological phenomena in focus*, Vol. 4. Elsevier.

Bonito, A., Picasso, M. and Laso, M., 2006. "Numerical simulation of 3d viscoelastic flows with free surfaces". *Journal of Computational Physics*, Vol. 215, No. 2, pp. 691–716.

Brasseur, E., Fyrillas, M.M., Georgiou, G.C. and Crochet, M.J., 1998. "The time-dependent extrudate-swell problem of an oldroyd-b fluid with slip along the wall". *Journal of Rheology*, Vol. 42, No. 3, pp. 549–566.

Castillo, E., Baiges, J. and Codina, R., 2015. "Approximation of the two-fluid flow problem for viscoelastic fluids using the level set method and pressure enriched finite element shape functions". *Journal of Non-Newtonian Fluid Mechanics*, Vol. 225, pp. 37–53.

Choi, H.C., Song, J.H. and Yoo, J.Y., 1988. "Numerical simulation of the planar contraction flow of a giesekus fluid". *Journal of Non-Newtonian Fluid Mechanics*, Vol. 29, pp. 347–379.

Comminal, R., Pimenta, F., Hattel, J.H., Alves, M.A. and Spangenberg, J., 2017. "Numerical simulation of the planar extrudate swell of pseudoplastic and viscoelastic fluids with the streamfunction and the vof methods". *Journal of Non-Newtonian Fluid Mechanics*.

Crochet, M. and Keunings, R., 1982. "Finite element analysis of die swell of a highly elastic fluid". *Journal of Non-Newtonian Fluid Mechanics*, Vol. 10, No. 3-4, pp. 339–356.

Deganello, D., Williams, A., Croft, T., Lubansky, A., Gethin, D. and Claypole, T., 2011. "Level-set method for the modelling of liquid bridge formation and break-up". *Computers & Fluids*, Vol. 40, No. 1, pp. 42–51.

Dou, H.S., Khoo, B.C., Phan-Thien, N., Yeo, K.S. and Zheng, R., 2007. "Simulations of fibre orientation in dilute suspensions with front moving in the filling process of a rectangular channel using level-set method". *Rheologica acta*, Vol. 46, No. 4, pp. 427–447.

Ferrás, L., Afonso, A., Alves, M., Nóbrega, J., Carneiro, O. and Pinho, F., 2014. "Slip flows of newtonian and viscoelastic fluids in a 4: 1 contraction". *Journal of Non-Newtonian Fluid Mechanics*, Vol. 214, pp. 28–37.

Figueiredo, R., Oishi, C., Afonso, A., Tasso, I. and Cuminato, J., 2016. "A two-phase solver for complex fluids: Studies of the weissenberg effect". *International Journal of Multiphase Flow*, Vol. 84, pp. 98–115.

Guénette, R. and Fortin, M., 1995. "A new mixed finite element method for computing viscoelastic flows". *Journal of non-newtonian fluid mechanics*, Vol. 60, No. 1, pp. 27–52.

Harlow, F.H. and Welch, J.E., 1965. "Numerical calculation of time-dependent viscous incompressible flow of fluid with free surface". *The physics of fluids*, Vol. 8, No. 12, pp. 2182–2189.

Hirt, C.W. and Nichols, B.D., 1981. "Volume of fluid (vof) method for the dynamics of free boundaries". *Journal of computational physics*, Vol. 39, No. 1, pp. 201–225.

Housiadas, K.D., Klidis, G. and Tsamopoulos, J., 2007. "Two-and three-dimensional instabilities in the film blowing process". *Journal of non-newtonian fluid mechanics*, Vol. 141, No. 2-3, pp. 193–220.

Irfan, M. and Muradoglu, M., 2017. "A front tracking method for direct numerical simulation of evaporation process in a multiphase system". *Journal of Computational Physics*, Vol. 337, pp. 132–153.

Janßen, C.F., Grilli, S.T. and Krafczyk, M., 2013. "On enhanced non-linear free surface flow simulations with a hybrid lbm–vof model". *Computers & Mathematics with Applications*, Vol. 65, No. 2, pp. 211–229.

Kim, M.S. and Lee, W.I., 2003. "A new vof-based numerical scheme for the simulation of fluid flow with free surface. part i: New free surface-tracking algorithm and its verification". *International Journal for Numerical Methods in Fluids*, Vol. 42, No. 7, pp. 765–790.

Kohno, H. and Tanahashi, T., 2004. "Numerical analysis of moving interfaces using a level set method coupled with adaptive mesh refinement". *International Journal for Numerical Methods in Fluids*, Vol. 45, No. 9, pp. 921–944.

Konaganti, V.K., Ansari, M., Mitsoulis, E. and Hatzikiriakos, S.G., 2015. "Extrudate swell of a high-density polyethylene melt: Ii. modeling using integral and differential constitutive equations". *Journal of Non-Newtonian Fluid Mechanics*, Vol. 225, pp. 94–105.

Kupferman, R., 2001. "A central-difference scheme for a pure stream function formulation of incompressible viscous flow". *SIAM Journal on Scientific Computing*, Vol. 23, No. 1, pp. 1–18.

Moraga, N.O., Lemus, L.A., Saavedra, M.A. and Lemus-Mondaca, R.A., 2015. "Vof/fvm prediction and experimental validation for shear-thinning fluid column collapse". *Computers & Mathematics with Applications*, Vol. 69, No. 2, pp. 89–100.

Muradoglu, M. and Tasoglu, S., 2010. "A front-tracking method for computational modeling of impact and spreading of viscous droplets on solid walls". *Computers & Fluids*, Vol. 39, No. 4, pp. 615–625.

Oishi, C., Martins, F., Tomé, M.F., Cuminato, J. and Mckee, S., 2011. "Numerical solution of the extended pom-pom model for viscoelastic free surface flows". *Journal of Non-Newtonian Fluid Mechanics*, Vol. 166, No. 3-4, pp. 165–179.

Osher, S. and Fedkiw, R.P., 2001. "Level set methods: an overview and some recent results". *Journal of Computational physics*, Vol. 169, No. 2, pp. 463–502.

Osher, S. and Sethian, J.A., 1988. "Fronts propagating with curvature-dependent speed: algorithms based on hamilton-jacobi formulations". *Journal of computational physics*, Vol. 79, No. 1, pp. 12–49.

Pivello, M.R., Villar, M., Serfaty, R., Roma, A. and Silveira-Neto, A., 2014. "A fully adaptive front tracking method for the simulation of two phase flows". *International Journal of Multiphase Flow*, Vol. 58, pp. 72–82.

Rajagopalan, D., Armstrong, R.C. and Brown, R.A., 1990. "Finite element methdos for calculation of steady, viscoelastic flow using constitutive equations with a newtonian viscosity". *Journal of Non-Newtonian Fluid Mechanics*, Vol. 36, pp. 159–192.

Ren, J., Ouyang, J. and Jiang, T., 2015. "An improved particle method for simulation of the non-isothermal viscoelastic fluid mold filling process". *International Journal of Heat and Mass Transfer*, Vol. 85, pp. 543–560.

Russo, G. and Phillips, T.N., 2010. "Numerical prediction of extrudate swell of branched polymer melts". *Rheologica acta*, Vol. 49, No. 6, pp. 657–676.

Sadek, S.H. and Yildiz, M., 2013. "Modeling die swell of second-order fluids using smoothed particle hydrodynamics". *Journal of Fluids Engineering*, Vol. 135, No. 5, p. 051103.

Sethian, J.A., 2001. "Evolution, implementation, and application of level set and fast marching methods for advancing fronts". *Journal of computational physics*, Vol. 169, No. 2, pp. 503–555.

Sridhar, T., Gupta, R., Boger, D. and Binnington, R., 1986. "Steady spinning of the oldroyd fluid b ii: Experimental results". *Journal of non-newtonian fluid mechanics*, Vol. 21, No. 1, pp. 115–126.

Sussman, M., Smereka, P. and Osher, S., 1994. "A level set approach for computing solutions to incompressible two-phase flow". *Journal of Computational physics*, Vol. 114, No. 1, pp. 146–159.

Tanner, R., 1970. "A theory of die-swell". *Journal of Polymer Science Part B: Polymer Physics*, Vol. 8, No. 12, pp. 2067–2078.

Terashima, H. and Tryggvason, G., 2009. "A front-tracking/ghost-fluid method for fluid interfaces in compressible flows". *Journal of Computational Physics*, Vol. 228, No. 11, pp. 4012–4037.

Tian, Z.F. and Yu, P., 2011. "An efficient compact difference scheme for solving the streamfunction formulation of the incompressible navier–stokes equations". *Journal of Computational Physics*, Vol. 230, No. 17, pp. 6404–6419.

Tomé, M., Castelo, A., Murakami, J., Cuminato, J., Minghim, R., Oliveira, M., Mangiavacchi, N. and McKee, S., 2000. "Numerical simulation of axisymmetric free surface flows". *Journal of Computational Physics*, Vol. 157, No. 2, pp. 441–472.

Tomé, M., Grossi, L., Castelo, A., Cuminato, J., McKee, S. and Walters, K., 2007. "Die-swell, splashing drop and a numerical technique for solving the oldroyd b model for axisymmetric free surface flows". *Journal of non-newtonian fluid mechanics*, Vol. 141, No. 2-3, pp. 148–166.

Tomé, M.F., Bertoco, J., Oishi, C.M., Araujo, M., Cruz, D., Pinho, F. and Vynnycky, M., 2016. "A finite difference technique for solving a time strain separable k-bkz constitutive equation for two-dimensional moving free surface flows". *Journal of Computational Physics*, Vol. 311, pp. 114–141.

Tomé, M.F., Castelo, A., Afonso, A.M., Alves, M. and Pinho, F.T.d., 2012. "Application of the log-conformation tensor to three-dimensional time-dependent free surface flows". *Journal of Non-Newtonian Fluid Mechanics*, Vol. 175, pp. 44–54.

Tryggvason, G., Bunner, B., Esmaeeli, A., Juric, D., Al-Rawahi, N., Tauber, W., Han, J., Nas, S. and Jan, Y.J., 2001. "A front-tracking method for the computations of multiphase flow". *Journal of Computational Physics*, Vol. 169, No. 2, pp. 708–759.

Ville, L., Silva, L. and Coupez, T., 2011. "Convected level set method for the numerical simulation of fluid buckling". *International Journal for numerical methods in fluids*, Vol. 66, No. 3, pp. 324–344.

Wang, K., 2013. "A new discrete evss method for the viscoelastic flows". *Computers & Mathematics with Applications*, Vol. 65, No. 4, pp. 609–615.

Wang, Y., Do-Quang, M. and Amberg, G., 2017. "Impact of viscoelastic droplets". *Journal of Non-Newtonian Fluid Mechanics*, Vol. 243, pp. 38–46.

Xu, X. and Yu, P., 2018. "A technique to remove the tensile instability in weakly compressible sph". *Computational Mechanics*, pp. 1–28.

Xue, S.C., Phan-Thien, N. and Tanner, R., 1998. "Three dimensional numerical simulations of viscoelastic flows through planar contractions". *Journal of Non-Newtonian Fluid Mechanics*, Vol. 74, No. 1-3, pp. 195–245.

Yi, W., Corbett, D. and Yuan, X.F., 2016. "A sharp-interface cartesian grid method for viscoelastic fluid flow in complex geometry". *Journal of Non-Newtonian Fluid Mechanics*, Vol. 234, pp. 82–104.

Zhang, Q., 2013. "On a family of unsplit advection algorithms for volume-of-fluid methods". *SIAM Journal on Numerical*

Analysis, Vol. 51, No. 5, pp. 2822–2850.

Zhuang, X., Ouyang, J., Li, W. and Li, Y., 2017. "Three-dimensional simulations of non-isothermal transient flow and flow-induced stresses during the viscoelastic fluid filling process". *International Journal of Heat and Mass Transfer*, Vol. 104, pp. 374–391.

7. RESPONSIBILITY NOTICE

The authors are the only responsible for the printed material included in this paper.